

Imaging and time-resolved study of laser-induced fluorescence of dysprosium atoms injected into superfluid helium

P. Moroshkin^{1,2,*} and K. Kono^{1,3}

¹RIKEN, CEMS, 2-1 Hirosawa, Wako, Saitama 351-0198, Japan

²Okinawa Institute of Science and Technology, 1919-1 Tancha, Onna-son, Okinawa 904-0495, Japan

³International College of Semiconductor Technology, National Chiao Tung University, Hsinchu 300, Taiwan



(Received 23 October 2019; revised manuscript received 5 April 2020; accepted 7 April 2020; published 28 April 2020)

We study the time evolution of the cloud of Dy atoms dispersed in superfluid helium and investigate the possibility of using these atoms as tracers for the imaging of superfluid-helium flows. The atoms are produced by pulsed laser ablation and are visualized via their laser-induced fluorescence. It turns out that the observation time is limited by the optical pumping of the atomic population into a nonabsorbing metastable state which is also responsible for the saturation of the fluorescence yield observed earlier.

DOI: [10.1103/PhysRevB.101.134520](https://doi.org/10.1103/PhysRevB.101.134520)

I. INTRODUCTION

Imaging the motion of tracer particles moving together with the liquid is a powerful method to visualize the liquid flow. It has been used in the studies of various systems, including quantum fluid ^4He . Introduction of the tracer particles into this cryogenic liquid represents a major experimental challenge. Typically, micron-sized solid hydrogen, deuterium, or frozen air particles are used in visualization studies of thermal counterflow, quantized vortices, and quantum turbulence in superfluid He [1–8].

A good tracer should be an efficient scatterer of the visible light and at the same time be as small as possible in order to minimize the disturbance of the liquid flow. It is also important that the tracers have a well-defined size and shape and are not heated by the illuminating light since the heat dissipation may significantly affect the liquid flow in the vicinity. From this perspective, single atoms and molecules of certain species are considered promising candidates for the flow visualization studies in superfluid helium. Another advantage of the atomic and molecular tracers is that their laser-induced fluorescence usually has a wavelength shifted with respect to that of the excitation laser. This enables an efficient spectral filtering and suppression of the unwanted scattered laser light from the sample cell walls, windows, and density fluctuations of the liquid.

A cloud of impurity atoms suspended in superfluid He was imaged for the first time in the pioneering experiments by the Heidelberg group [9,10]. In those experiments, Ba^+ , Mg^+ , and Tl^+ ions were injected into superfluid ^4He and then recombined with free electrons produced by a field emission tip. The fluorescence emitted by the resulting cloud of electronically excited atoms was imaged and provided

information about the drift velocity of the ions in the external electric field.

Fluorescing He_2^* excimer quasimolecules were used as tracers for the visualization of the counterflow in superfluid helium [11–14]. The excimers in a metastable $a^3\Sigma_u$ state were produced either by an electric discharge near a high-voltage tip or by a laser breakdown in liquid He induced by focused femtosecond laser pulses. The cloud of excimers was imaged using the laser-induced fluorescence excited via an infrared two-photon $a^3\Sigma_u - d^3\Sigma_u$ transition.

Optical spectra of many atomic and molecular impurities in liquid and solid He matrices are strongly broadened by the interaction with surrounding helium (for a review see [15]). This spectral broadening greatly reduces the absorption probability for the resonant laser radiation, which leads to a low fluorescence yield and poses a serious problem for the imaging studies. Inner-shell $5f-4d$ electronic transitions of lanthanide elements are much less broadened due to the screening effect of the electrons in the outer $6s$ shell [16–19]. These transitions are therefore much better suited for imaging.

In our recent publications [18,19] we investigated the absorption spectrum of the $^5I_8 - ^5K_7$ inner-shell transition of Dy atoms in superfluid helium and confirmed its exceptionally small spectral width. Here, we present an extension of that study and report the imaging of the Dy atomic cloud in liquid helium using the laser-induced fluorescence. We investigate the dynamics of the laser-induced fluorescence and the saturation of the fluorescence yield at a high excitation laser power.

II. EXPERIMENT

A. Experimental setup

The experimental setup is described in our recent publication [19]. The experiments are carried out in an optical helium-bath cryostat cooled to 1.35–2.1 K by pumping on the helium bath. The side view of the sample cell and the configuration of the laser beams are shown Fig. 1.

*Present address: Brown University, School of Engineering, Providence, Rhode Island 02912, USA; petr_moroshkin@brown.edu

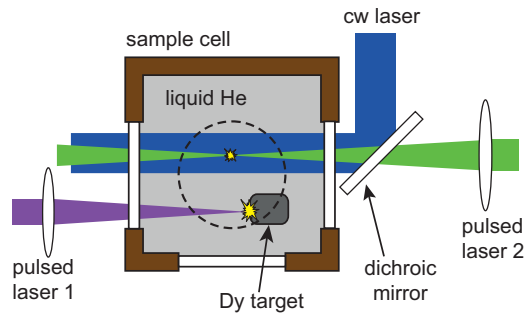


FIG. 1. Side view of the experimental sample cell.

Superfluid He in the sample cell is doped with dysprosium atoms by means of laser ablation using two nanosecond pulsed lasers. The primary ablation of a metallic Dy target by a frequency-tripled DPSS laser ($\lambda = 355$ nm) produces mostly metal clusters and nanoparticles. Dy atoms are produced by the secondary ablation and sputtering of these nanoparticles by another, more powerful pulsed laser. The primary ablation laser has a repetition rate of 20–100 Hz and a pulse energy of $70 \mu\text{J}$. It is expanded to a diameter of 2 cm and then focused on the target by a $f = 15$ cm lens mounted on a motorized XY translation stage that is moving in a plane orthogonal to the laser beam. In this way we move the ablation spot along the target surface within an area of 2×1 mm, thus avoiding drilling of a crater. For the secondary sputtering we use either a frequency-doubled Nd:yttrium aluminum garnet (YAG) laser ($\lambda = 532$ nm) with a maximum repetition rate of 10 Hz and a pulse energy of 0.5–15 mJ or a frequency-tripled Nd:YAG laser ($\lambda = 355$ nm) with a maximum repetition rate of 20 Hz and a pulse energy of 1.5–6.5 mJ. The secondary laser beam is expanded to a diameter of 2.5 cm and then focused in the middle of the sample cell, above the Dy target, as shown in Fig. 1.

Dy atoms in liquid He are excited by a second harmonic of a tunable cw Ti:sapphire laser superimposed on the secondary sputtering laser beam using a dichroic mirror. For the spectroscopy studies, we use an approximately parallel or slightly converging cw laser beam. For the imaging experiments, the beam was expanded by a telescope up to a diameter of 2–5 mm and was significantly broader than the secondary pulsed laser beam over the whole length of the sample cell (see Fig. 1). Laser-induced fluorescence is collected at a right angle with respect to the laser beams and is analyzed with a grating spectrograph equipped with a CCD camera and a photomultiplier tube (PMT).

The ablation process is monitored with a high-speed digital complementary metal-oxide semiconductor (CMOS) video camera oriented orthogonal to the laser beams and operated at a frame rate of 500–8500 fps. The camera is equipped with a macro-objective with adjustable focal distance and magnification ≤ 1 . In Fig. 2 we show selected frames from a typical video recording made via a side window. The interior of the cell is illuminated by a collimated beam of a powerful LED shining through the opposite side window.

For the imaging of the atomic fluorescence we use either the same high-speed CMOS camera or a thermoelectrically cooled CCD camera. In both cases the image is produced

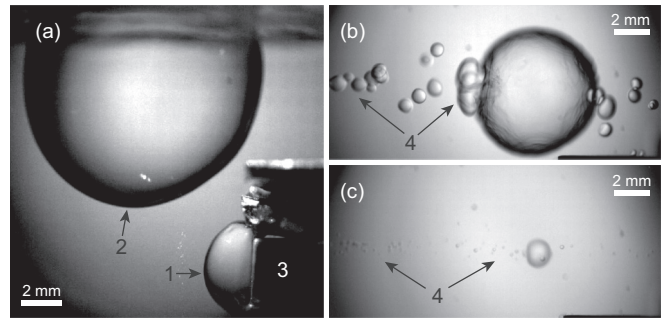


FIG. 2. Selected frames from three high-speed video recordings showing laser-induced gas bubbles in liquid He. 1, a bubble at the primary ablation spot; 2, a bubble due to the breakdown in the secondary laser focus; 3, ablation target; 4, a string of small bubbles along the secondary laser beam. Each picture corresponds to the moment when the bubbles reach their largest size. Exposure time is 1.6 ms. (a) $T = 1.35$ K, delay time with respect to the secondary laser pulse $\tau = 11.4$ ms, pulse energy $W_{\text{Las}} = 11.5$ mJ; (b) $T = 2.06$ K, $\tau = 3.2$ ms, $W_{\text{Las}} = 14$ mJ; and (c) $T = 2.06$ K, $\tau = 1.6$ ms, $W_{\text{Las}} = 7.0$ mJ.

by the same macro objective. The scattered light from all three laser beams was suppressed by a low-pass interference filter with a cutoff wavelength of 600 nm. Due to the low fluorescence intensity, the CMOS camera had to be operated at a relatively low frame rate of 10–50 frames/s. The CCD camera was used to take still images of the atomic cloud at a chosen delay time with respect to the secondary sputtering laser pulse with an exposure time of 1–100 ms.

B. Microparticles and laser-induced gas bubbles

In Fig. 2(a) one can see a typical image of gas bubbles produced by the laser ablation at the lowest accessible temperature of 1.35 K. There is a hemispherical gas bubble centered at the primary ablation spot on the target surface. It expands and collapses over ≈ 10 ms following each primary ablation laser pulse. The bubble reaches a maximum diameter of ≈ 5 mm and does not perturb the sample volume illuminated by the cw laser beam.

Another gas bubble is formed in the middle of the cell when the secondary sputtering laser pulse hits a metallic particle passing through its focal region. The image in Fig. 2(a) corresponds to a large laser pulse energy, $W_{\text{Las}} \gtrsim 10$ mJ. Under these conditions, we obtain a laser breakdown in liquid He in the laser focus accompanied by a bright flash of light containing spectral lines of He atoms and He_2^* excimers. The breakdown is followed by the rapid growth of a large spherical gas bubble reaching a diameter of 5–20 mm, as shown in Fig. 2(a). The bubble growth and collapse take 10–20 ms and strongly affect the measurements of the laser-induced fluorescence from Dy atoms.

Since the helium in the sample cell is always under a saturated vapor pressure, the increase in the helium temperature from 1.35 to 2.1 K leads to the pressure increase from 200 to 4000 Pa. This external pressure applied to the liquid has a pronounced effect on the laser-induced bubbles. At a higher temperature, the lifetime of the bubble and its maximal radius become 2–3 times shorter than at $T = 1.35$ K. This effect is

illustrated in Fig. 2(b), showing the secondary bubble at its largest expansion at $T = 2.06$ K. One can also see a string of smaller bubbles along the track of the secondary laser beam. We expect that each of the smaller bubbles corresponds to a Dy nano- or microparticle heated and probably destroyed by the secondary laser pulse. Formation of similar small gas bubbles around injected nanoparticles was studied in detail in [20].

The largest and most stable Dy fluorescence yield was achieved at a moderate secondary pulse energy $W_{\text{Las}} = 3\text{--}7$ mJ, below the breakdown threshold. A typical image is shown in Fig. 2(c). Under these conditions no large bubble is produced in the laser focus. We still observe a string of very small bubbles appearing along the track of the secondary pulsed laser beam. Their diameters do not exceed 0.5 mm, and the bubbles disappear typically within 2 ms. The laser-induced fluorescence spectra reported below and in [18,19] were obtained in this regime.

With the primary ablation laser operated at a repetition rate of 20 Hz or more, the cell quickly becomes filled with metallic nano- and microparticles. The particles efficiently scatter the laser light and therefore can be visualized using an expanded cw laser beam and the video camera [21,22]. By moving the cw laser beam across the sample cell in both horizontal and vertical directions we have verified that the entire sample volume is filled with the particles. Their motion is affected very little by the expanding and collapsing gas bubbles. The particles slowly drift in random directions. Near the target, they seem to follow the flow of the normal-fluid component arising due to the counterflow excited by the inhomogeneous heating of the ablation target by the laser pulses. It is directed predominantly away from the target and is strongly inhomogeneous and turbulent, with many large-scale eddies appearing and disappearing on the timescale of several milliseconds.

C. Laser-induced fluorescence spectrum

A typical spectrum of the laser-induced fluorescence recorded by the spectrograph with the CCD camera is shown in Fig. 3. The emission is excited by the Ti:sapphire laser tuned into the resonance with the transition from the $4f^{10}6s^2$ 5I_8 ground state of Dy towards the state $4f^9 5d6s^2$ 5K_7 at $\lambda = 458.9$ nm (see Fig. 4). By selecting the delay time between the ablation laser pulse and the CCD exposure time, we have verified that this emission is produced by the Dy atoms solvated in superfluid He. The Dy atoms in the primary ablation plume and in the gas bubbles appearing in the focus of the secondary sputtering laser beam emit much narrower spectral lines and do not contribute to the spectrum in Fig. 3.

In total we observe seven spectral lines originating from the electronic states of Dy lying below the laser-excited $4f^9 5d6s^2$ 5K_7 state. The corresponding transitions are shown in Fig. 4 by solid red arrows and are listed in Table I. Their line shapes are discussed in detail in [18]. The observed transitions are indicated in Fig. 4 by the red arrows. The emission spectrum is dominated by a strong line at 641 nm (labeled 5 in Fig. 3) which originates from the state $(^5I_8)(^3P_0)$, the lowest in the group of $4f^{10}6s6p$ $(^5I_8)(^3P_k)$ states (see Fig. 4). In a free Dy atom this transition has wavelength $\lambda_{\text{free}} = 642.4$ nm. We

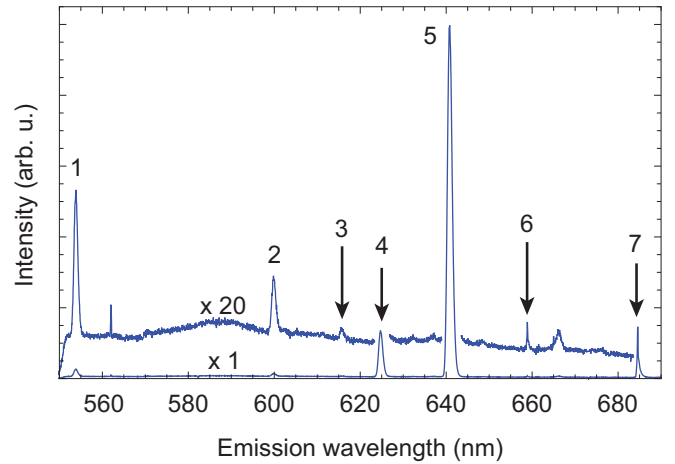


FIG. 3. Laser-induced fluorescence spectrum. Excitation at $\lambda_{\text{Las}} = 458.9$ nm. Numbers 1 to 7 mark the emission lines of Dy (see Fig. 4).

also observe the emission from two other $4f^{10}6s6p$ $(^5I_8)(^3P_k)$ states (lines 1 and 4 in Fig. 3) and from two higher-lying $4f^{10}6s6p$ $(^5I_7)(^3P_k)$ states (lines 2 and 3 in Fig. 3). All these emission lines are strongly broadened and blueshifted, which is typical for the valence electron transitions [15,23].

In the emission spectrum we also observe two transitions from states 5H_7 and 5I_8 belonging to the configuration $4f^9 5d6s^2$ (6 and 7 in Fig. 3; $\lambda_{\text{free}} = 657.9$ and 683.5, respectively). These two inner-shell transitions are much less broadened and are shifted in the opposite direction.

D. Time-resolved fluorescence

Typical time-resolved fluorescence signals at $\lambda_{\text{emiss}} = 641$ nm measured by the PMT are shown in Fig. 5. Here, curve 1 is

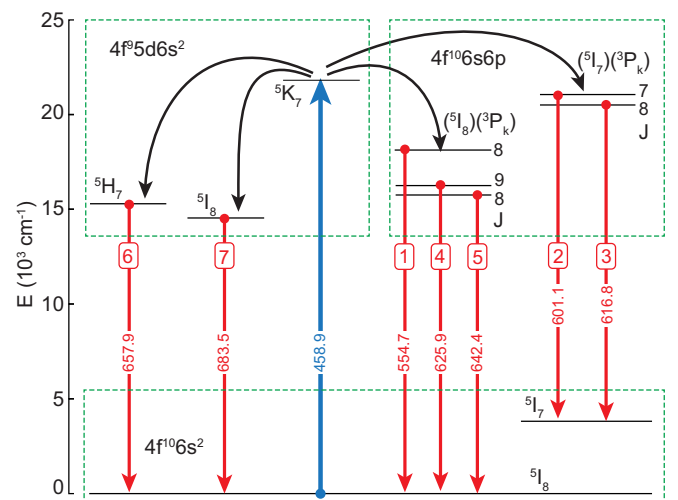


FIG. 4. Electronic states and transitions of a Dy atom [24]. Only the states and transitions that are relevant for the present work are shown. The vertical blue arrow indicates the transition excited by the laser. Red arrows indicate the transitions observed in the fluorescence spectrum, numbered according to Fig. 3 (see also Table I). Transition wavelengths are given in nanometers.

TABLE I. Parameters of electronic transitions of Dy atoms observed in the present experiment. The wavelengths of the free Dy atom λ_{free} , spontaneous emission rates A_{ki} , and statistical weights of the upper g_k and lower g_i electronic states are taken from [24]. f_{ik} are the oscillator strengths from [39]. I_{rel} represent relative intensities observed in the present work in the emission spectrum. The last column shows the labels assigned to the transitions in Figs. 3 and 4.

Transition	λ_{free} (nm)	A_{ki} (s^{-1})	f_{ik} (10^{-3})	g_i	g_k	I_{rel}	Label
$(^5I_8)(^3P_2)-^5I_8$	554.7	3.0×10^5	1.8	17	17	0.017	1
$(^5I_7)(^3P_1)-^5I_7$	601.1	5.9×10^5	10	15	15	0.007	2
$(^5I_7)(^3P_1)-^5I_7$	616.8	8.1×10^5	11	15	17	0.002	3
$(^5I_8)(^3P_1)-^5I_8$	625.9	8.9×10^5	5.4	17	19	0.113	4
$(^5I_8)(^3P_0)-^5I_8$	642.2		1	17	17	1.00	5
$^5K_7-^5I_8$	458.9	1.37×10^7	40	17	15		
$^5H_7-^5I_8$	657.9	7.7×10^5	4.7	17	15	0.002	6
$^5I_8-^5I_8$	683.5			17	17	0.052	7

obtained with the cw excitation laser blocked and represents the emission from the laser-induced plasma in the focus of the secondary pulsed laser beam. The pulse width is limited by the detector bandwidth. Curve 2 shows the emission excited by the cw Ti:sapphire laser tuned to $\lambda_{\text{Las}} = 458.9$ nm, in resonance with the Dy absorption line.

Following the secondary sputtering laser pulse, the atomic fluorescence excited by the cw laser increases over ≈ 5 ms, reaches a maximum, and then decreases exponentially with decay time $\tau \approx 90$ ms. The rise time is similar to the typical lifetime of large gas bubbles appearing in the focus of the pulsed laser at a large laser power. The increase in the atomic fluorescence yield thus can be associated with the collapse of the gas bubble and to the increase in the number of Dy atoms solvated in liquid He. The decay of the fluorescence yield at larger delay times may be attributed to the diffusion

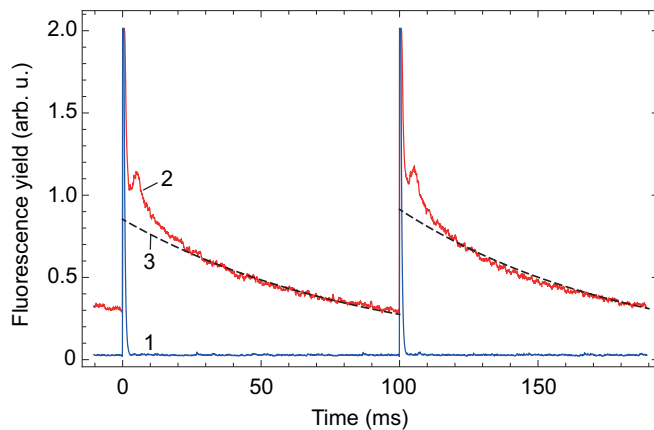


FIG. 5. Time-resolved emission intensity at $\lambda_{\text{emiss}} = 641$ nm. $T = 1.35$ K, secondary sputtering laser: $\lambda = 532$ nm, $W_{\text{Las}} = 4.5$ mJ, pulses at $t = 0$ and 100 ms. Curve 1 (blue), cw excitation laser blocked; curve 2 (red), cw excitation at $\lambda_{\text{Las}} = 458.9$ nm, $P_{\text{Las}} = 9.0$ mW; curve 3 (black dashed), exponential fit to the data at $t = 20$ –100 and 120–190 ms.

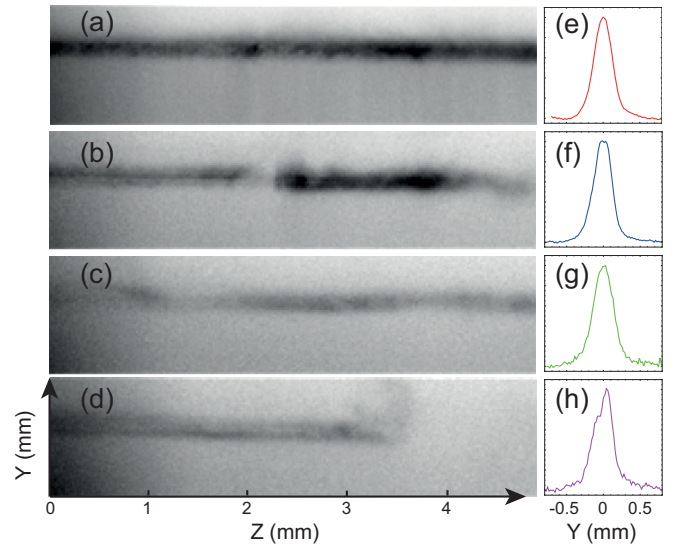


FIG. 6. (a)–(d) Images of laser-induced fluorescence made with the CCD camera. (e)–(h) Corresponding transversal profiles of the atomic cloud. Camera exposure time in (a) 10 ms and in (b)–(d) 100 ms. Delay time with respect to the secondary laser pulse: (a) and (e) $\tau = 0$, (b) and (f) $\tau = 5$ ms, (c) and (g) $\tau = 100$ ms, and (d) and (h) $\tau = 200$ ms. $T = 2.07$ K; secondary laser pulse energy $W_{\text{Las}} = 3$ mJ, cw laser power $P_{\text{Las}} = 22$ mW.

of the Dy atoms from the excitation zone illuminated by the cw laser beam or to the coalescence of the atoms into dimer molecules and clusters. However, our estimates of the diffusion coefficient (Sec. III A) and of the atomic density (Sec. III B) rule out both these interpretations. Alternatively, the observed dynamics can be a result of optical pumping that transfers the Dy atoms to a nonabsorbing metastable state. The latter interpretation is discussed in detail in Sec. III C.

E. Imaging of the atomic fluorescence

In Figs. 6(b)–6(d) we show images of the atomic Dy fluorescence excited by the cw Ti:sapphire laser at 458.9 nm, $P_{\text{Las}} = 20$ mW, $T = 2.0$ K. The secondary sputtering laser ($\lambda = 532$ nm) is operated at a repetition rate of 2 Hz and a pulse energy of 3.0 mJ. The images are taken by the CCD camera with the exposure time of 100 ms delayed with respect to the laser pulse by $\tau_d = 5, 100,$ and 200 ms. The fluorescence is produced along the track of the secondary pulsed laser beam with a diameter (FWHM) equal to 0.3 mm. Note that the diameter of the cw laser beam at the center of sample volume is ≈ 4 mm.

The diameter of the track does not change with the increased delay time. In Figs. 6(f)–6(h) we plot the transversal distribution of the light intensity across the track binned over a length of 2 mm (100 pixels). The same track diameter was also obtained with a camera exposure time of 10 ms, overlapping with the laser pulse [Figs. 6(a) and 6(e)]. No noticeable spread of the atomic cloud due to the diffusion occurs on a time interval of 300 ms. The observed decay of the laser-induced fluorescence (see Fig. 5) thus does not result from the spread of the atomic cloud.

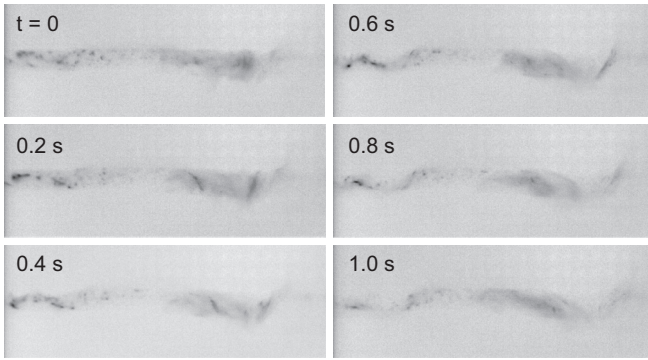


FIG. 7. Selected frames from a video recording of atomic fluorescence made by the CMOS camera. Exposure time of each frame is 50 ms; image size is 12×4 mm. $T = 1.4$ K, secondary laser pulse energy $W_{\text{Las}} = 7$ mJ, repetition rate is 10 Hz, and cw laser power $P_{\text{Las}} = 70$ mW.

The images of the atomic cloud shown in Fig. 6 represent single exposures, each synchronized to the nearest preceding secondary sputtering laser pulse. The whole sequence is taken within a time interval of several minutes, with a number of laser pulses fired between the successive images. Because of relatively quiet conditions (low laser pulse energy), the shape of the cloud does not change on this timescale. Images obtained by the accumulation of many exposures demonstrate the same profile of the track. However, the brightness of the atomic fluorescence along the track is not always uniform, as can be seen in Figs. 6(a)–6(d). The effect becomes more pronounced at a higher power and repetition rate of the pulsed laser.

The dynamics of the atomic cloud is relatively slow and can be observed in the video recordings made by the CMOS camera. Selected frames from a typical video recording made at $W_{\text{Las}} = 7$ mJ and a repetition rate of 10 Hz are shown in Fig. 7. The cw laser power is also increased to 70 mW. The delay time is indicated in each frame. Each exposure overlaps with one secondary laser pulse; therefore, no decay of the emission brightness can be seen. The shape of the emitting atomic cloud does not follow exactly the straight path of the secondary laser beam. One can also see a pronounced inhomogeneity of the emission intensity within the atomic cloud.

The shape of the cloud and the structure of the bright spots evolve relatively slowly, on a timescale of seconds. Both are only weakly affected by every successive laser pulse. This would be impossible if the atoms completely disappeared during the time interval between the two pulses and each successive pulse created an entirely new atomic cloud. On the other hand, the observations are consistent with the following scenario. The atoms become invisible because they stop absorbing the cw laser light at $\lambda = 458.9$ nm and emit no fluorescence. At the same time, they move very slowly and remain within the excitation zone until the arrival of the next secondary laser pulse. The interaction with the intense laser pulse at $\lambda = 532$ or 355 nm transfers the atoms back into the absorbing state and thus makes them visible again.

We attribute the slow motion of the atomic cloud to the effect of the macroscopic liquid-helium flow. The atoms

experience a drag force only from the normal-fluid component of superfluid He that possesses a finite viscosity. In the temperature range of our experiments, the normal-fluid fraction varies between 5% and 75% [25]. The motion of the Dy atomic cloud in Fig. 7 thus visualizes the flow of the normal-fluid component driven by the local heating by the intense laser beams (thermal counterflow) and/or by the gas bubble dynamics.

It is expected that impurity atoms in superfluid He can be trapped by quantized vortices, similar to the trapping of micron-sized tracer particles [1,2], free electrons (electron bubbles), [26,27] and positive ions [27]. However, in the images obtained in the present experiments we could not identify any objects resembling vortex lines decorated by trapped Dy atoms. The sensitivity of the camera and the resolution of the imaging system in the present experiment are not sufficient for resolving the individual Dy atoms.

III. ANALYSIS

As can be seen in Figs. 5 and 6, the atomic fluorescence observed in the experiment decays on a timescale of 50–100 ms, without the spreading of the atomic cloud. Below we discuss possible mechanisms leading to the loss of the Dy atoms: (i) diffusion of atoms out of the observation zone, (ii) their coalescence into dimer molecules and larger clusters and nanoparticles, and (iii) optical pumping into a long-lived nonabsorbing electronic state(s).

A. Diffusion of Dy atoms in liquid helium

Dy atoms produced along the track of the secondary sputtering laser beam are expected to spread out because of the diffusion. The excitation zone is defined by the cw Ti:sapphire laser beam. In the imaging study it had a diameter of ≈ 4 mm, i.e., much larger than that of the sputtering laser. One therefore could expect to see the spreading of the atomic cloud until it fills the cross section of the cw laser beam.

The rate of diffusion of impurity atoms in superfluid helium has not been measured. The diffusion coefficient D is expected to be of the same order of magnitude as that of He_2^* , which was estimated in [28]. In the temperature range of our experiments, $D(\text{He}_2^*) \sim 10^{-4}$ – 10^{-3} cm²/s [28]. Similar values of the diffusion coefficient have been obtained for spin-polarized ^3He impurity atoms in dilute ^4He – ^3He mixtures [29,30]. Residence times of various metal impurity atoms reported in spectroscopy experiments range from a few tens of milliseconds [31] to 500 ms [32,33] and even several seconds [34]. It was also suggested [34] that the atoms are removed from the observation zone not by diffusion, but rather by a convection or a counterflow arising due to the inhomogeneous heating by the ablation laser pulses.

$$\frac{\partial N_{at}}{\partial t} = \frac{1}{r} \frac{\partial}{\partial r} \left(r D \frac{\partial N_{at}}{\partial r} \right). \quad (1)$$

In order to model the diffusion of Dy atoms created within the approximately cylindrical volume illuminated by the pulsed laser beam, we find a solution of the diffusion equation (1) following the procedure described in [35]. The initial distribution of the atoms $N_{at}(r, t = 0)$ is modeled by a radial

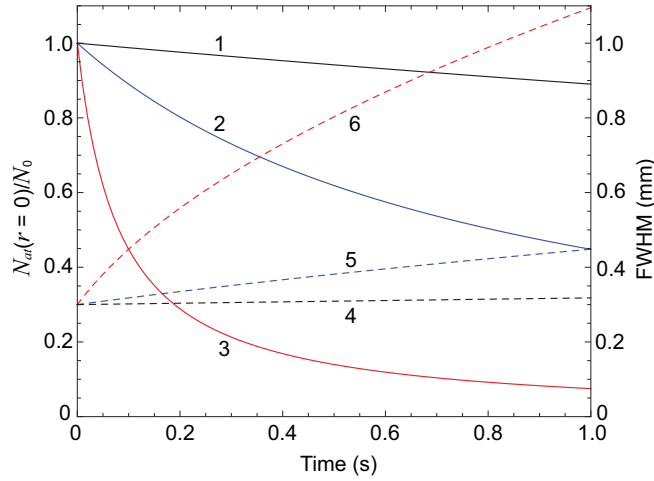


FIG. 8. Results of the calculations of the diffusion of impurity atoms in liquid He. Solid curves (left axis), normalized atomic density on the laser beam axis; dashed curves (right axis), FWHM diameter of the atomic cloud. Curves 1 and 4, $D = 10^{-5}$ cm²/s; curves 2, 5, $D = 10^{-4}$ cm²/s; curves 3, 6, $D = 10^{-3}$ cm²/s.

Gaussian function with a FWHM of 0.3 mm, corresponding to Fig. 6(e):

$$N_{at}(r, t = 0) = N_0 \exp\left(-\frac{r^2}{w^2}\right). \quad (2)$$

The time-dependent concentration of the impurity atoms $N_{at}(r, t)$ is found as

$$N_{at}(r, t) = \frac{2}{a^2} \sum_{k=1}^n C_k \exp(-D\alpha_k^2 t) J_0(\alpha_k r), \quad (3)$$

with the coefficients

$$C_k = \frac{1}{J_1(\alpha_k a)^2} \int_0^a N_{at}(r, t = 0) J_0(\alpha_k r) r dr. \quad (4)$$

Here, $J_0(x)$ and $J_1(x)$ are Bessel functions, a is the radius of the sample volume, and α_k are the roots of the equation $J_0(\alpha_k a) = 0$. It is assumed that the atoms reaching $r = a$ stick to the wall and disappear. In the geometry of our experiment ($a \gg w$), the terms up to $n = 130$ must be included in the summation in Eq. (3).

In Fig. 8 we show the calculated time dependence of the atomic density at the axis of the laser beam, $N_{at}(r = 0, t)/N_0$, and of the FWHM diameter of the atomic cloud for different values of D . Our experimental observations are consistent with the magnitude of the diffusion coefficient $D \leq 10^{-4}$ cm²/s. No significant spreading of the atomic cloud can be seen within the time interval of 200–300 ms following the sputtering laser pulse (see Fig. 6). This is also consistent with the data of [28,32–34]. The dominating loss mechanism is not associated with the diffusion.

B. Coalescence of Dy atoms into molecules and nanoparticles

Dy atoms solvated in superfluid helium may form dimer molecules and larger clusters. They may also attach themselves to nanoparticles that have survived the secondary laser sputtering. Both processes will lead to the decrease of the

density of solvated atoms and to a depletion of the laser-induced fluorescence.

The coalescence of two atoms or an atom and a larger particle is possible only upon a collision at a very close distance, and therefore, the rates of both reactions are controlled by the diffusion. For a diatomic recombination, the distance between the two atoms should be approximately equal to the diameter of the atomic bubble, $2R_b \approx 1$ nm [18]. The atomic density N_{at} obeys the following equation [36]:

$$\frac{dN_{at}}{dt} = -8\pi R_b D N_{at}^2. \quad (5)$$

The solution is

$$N_{at}(t) = \frac{N_0}{t/\tau_{at} + 1}. \quad (6)$$

The decay of $N_{at}(t)$ is nonexponential, with a characteristic decay time depending on the initial atomic density:

$$\tau_{at} = \frac{1}{8\pi R_b D N_0}. \quad (7)$$

In order to estimate the absolute value of N_0 achieved in the experiment, we use the expression for the absorption rate per atom [37]:

$$W_a = \frac{\lambda^3 A_{ik}}{8\pi h \Delta \nu c} \frac{g_k}{g_i} I_{Las}. \quad (8)$$

Here, A_{ik} is the Einstein coefficient for spontaneous emission (see Table I), g_i and g_k are the statistical weights of the ground and excited states, respectively, c is the speed of light, and h is the Planck constant. It is assumed that the cw laser with the intensity I_{Las} is tuned exactly at a center of the excitation spectrum that has a Lorentzian line shape with a FWHM width $\Delta \nu$. At a low laser power, the fluorescence yield is given by $I_F = W_a N_{at}$. By comparing the results of the calculation with the experimentally measured fluorescence yield corrected for the collection efficiency, we can estimate the atomic density: $N_0 \sim 10^8$ cm⁻³.

The diatomic coalescence time τ_{at} can thus be calculated using Eq. (7), assuming the value of the diffusion coefficient $D \leq 10^{-4}$ cm²/s obtained in Sec. III A: $\tau_{at} \geq 10$ s. It leads to a decay of the atomic density that is even slower than that resulting from the spreading of the atomic cloud.

The coalescence of atoms with larger particles is described by a rate equation similar to Eq. (5):

$$\frac{dN_{at}}{dt} = -4\pi(R_c + R_b)(D + D_c)N_c N_{at}, \quad (9)$$

where N_c is a number density of all particles larger than a single atom, R_c is the particle radius, and D_c is their diffusion coefficient. Since $R_c > R_b$, it is expected that $D_c < D$. The solution is

$$N_{at}(t) = N_0 \exp\left(-\frac{t}{\tau_c}\right), \quad (10)$$

$$\tau_c = \frac{1}{4\pi(R_c + R_b)(D + D_c)N_c} \simeq \frac{1}{4\pi R_c D N_c}. \quad (11)$$

The experimentally observed decay time of the atomic density (Fig. 5) can be attributed to the attachment of atoms to nanoparticles only if the product $N_c R_c$ exceeds 10^8 m⁻². Our

estimates [21] suggest that metallic nanoparticles with a diameter of about 100 nm or larger scatter a sufficient intensity of the laser light to be detected by our video camera. The number density of such particles can be estimated from our video recordings. Their contribution is totally negligible in comparison with the diatomic recombination. Smaller nanoparticles and atomic clusters ($1 \text{ nm} < R_c < 50 \text{ nm}$) remain invisible. They may produce the observed effect, but only if their number density is extremely high: $10^9\text{--}10^{11} \text{ cm}^{-3}$.

C. Saturation and optical pumping

The slow decay of atomic fluorescence following the sputtering laser pulse observed in the experiment (Fig. 5) may result from the optical pumping of Dy atoms into a long-lived electronic state that has no allowed transition to the ground state. The candidate metastable state can be easily identified in Fig. 4 as the $4f^{10}6s^2\ ^5I_7$ state that has an energy of 4134 cm^{-1} above the 5I_8 ground state. It is populated by the spontaneous emission at 601.1 and 616.8 nm (emission lines 2 and 3 in Fig. 3 and Table I). At present, nothing is known about its lifetime in a superfluid helium environment.

The rate at which the atomic population is pumped into the metastable state is determined by the intensity of the cw excitation laser I_{Las} and by the branching ratio between the emission lines terminating at the metastable and at the ground state. Below, we develop a rate-equation model that uses the results of our earlier work [18], where we have investigated the dependence of the fluorescence yield on the excitation laser power. In that experiment, a mean fluorescence intensity at each emission line was measured, averaged over a time much longer than the dynamics reported here in Figs. 5–7. As the power of the resonant cw laser is increased, the fluorescence yield I_F saturates according to

$$I_F \propto \frac{I_{\text{Las}}}{1 + I_{\text{Las}}/I_S^{\text{exp}}}. \quad (12)$$

Here, I_S^{exp} is the saturation intensity that is determined by fitting the experimental data. The same dependence was obtained by measuring the laser-induced fluorescence at different emission channels. The resulting saturation intensity for the excitation at the zero-phonon line (ZPL) of the $^5I_8\text{--}^5K_7$ transition increases with the temperature. At $T = 1.4 \text{ K}$, $I_S^{\text{exp}} = 17 \pm 5 \text{ mW/cm}^2$, and at $T = 2.05 \text{ K}$, $I_S^{\text{exp}} = 100 \pm 20 \text{ mW/cm}^2$.

Assuming a homogeneously broadened two-level atomic transition, the saturation intensity can be calculated [38] as

$$I_S^{(2)} = \frac{4\pi ch \Delta\nu}{\lambda^3} \frac{g_i}{g_k}, \quad (13)$$

which corresponds to the condition $W_a = A_{ik}/2$. Equation (13) can explain partially the observed increase of the saturation intensity with the temperature since the spectral width of the ZPL is also increasing from $\Delta\nu = 5.5 \text{ GHz}$ at $T = 1.4 \text{ K}$ to $\Delta\nu = 11.5 \text{ GHz}$ at $T = 2.1 \text{ K}$ [19]. However, the absolute value of the saturation intensity calculated using the measured value of $\Delta\nu$ [19] is $I_S^{(2)} \approx 10 \text{ W/cm}^2$, which is 600 times larger than the experimentally measured value I_S^{exp} . This discrepancy is also attributed to the optical pumping of the atomic population into the metastable state.

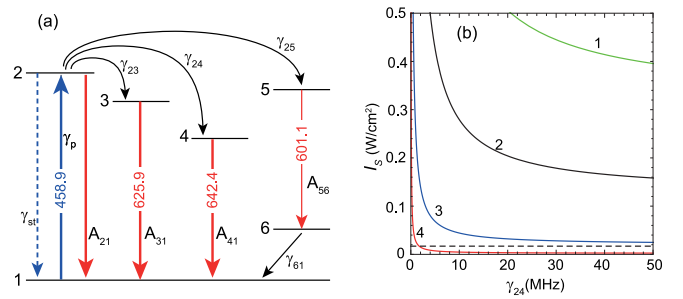


FIG. 9. (a) A simplified six-level system used to calculate the steady-state atomic populations. Blue, red, and black solid arrows represent optical excitation, spontaneous emission, and radiationless transitions, respectively; the dashed blue arrow indicates stimulated emission. (b) Calculated saturation intensity I_S as a function of the radiationless rate γ_{24} . Curve 1: $\gamma_{25} = 0$, states 5 and 6 not populated; curves 2, 3, and 4: $\gamma_{25} \neq 0$, $\gamma_{61} = 1000, 100$, and 10 s^{-1} , respectively.

We neglect all minor decay channels and consider the simplified six-level system shown in Fig. 9 (a). It includes the laser-excited transition at 458.9 nm, two transitions that are most prominent in the experimental emission spectrum at 642 and 626 nm, and the transition at 601 nm. The emission at 601 nm is rather weak. It has to be included since this transition leads to the population transfer to the 5I_7 state that is metastable and may become a trap for the excited atomic population (see Fig. 4). The steady-state populations of the six atomic states N_1 to N_6 can be found by solving the system of rate equations:

$$N_1\gamma_p = N_2(A_{21} + \gamma_{st}) + N_3A_{31} + N_4A_{41} + N_6\gamma_{61}, \quad (14)$$

$$N_2\gamma_{23} = N_3A_{31}, \quad (15)$$

$$N_2\gamma_{24} = N_4A_{41}, \quad (16)$$

$$N_2\gamma_{25} = N_5A_{56}, \quad (17)$$

$$N_6\gamma_{61} = N_5A_{56}, \quad (18)$$

$$N_1 + N_2 + N_3 + N_4 + N_5 + N_6 = 1. \quad (19)$$

Here, A_{21} , A_{31} , A_{41} , and A_{56} represent the spontaneous emission rates of states 2, 3, 4, and 5, respectively. A_{21} , A_{31} , and A_{56} can be found in [24] (see Table I). In order to determine A_{41} , we use measured the values of the relative oscillator strengths f_{ik} of Dy transitions reported in [39] (see Table I). Since $f_{ik} \propto A_{ki}g_k/g_i$, the absolute value of A_{41} is calculated as follows:

$$A_{41} = \frac{f_{14} g_2}{f_{12} g_4} A_{21}, \quad (20)$$

with the result $A_{41} \approx 1.7 \times 10^5 \text{ s}^{-1}$. γ_p and γ_{st} are the optical pumping and stimulated emission rates for state 2 [38]:

$$\gamma_p = \frac{A_{21}\lambda^3}{8\pi ch \Delta\nu} \frac{g_2}{g_1} I_{\text{Las}}, \quad (21)$$

$$\gamma_{st} = \gamma_p \frac{g_1}{g_2}. \quad (22)$$

The rates γ_{23} , γ_{24} , γ_{25} , and γ_{61} , corresponding to the radiationless transitions (see Fig. 9), are unknown and have to be found together with the state populations. It is expected that γ_{61} is much smaller than all other radiationless rates in the system due to the large energy separation of the two states and the absence of any intermediate states.

The populations of excited states 3, 4, and 5 are proportional to the experimentally observed intensities of the laser-induced fluorescence at the transitions $3 \rightarrow 1$, $4 \rightarrow 1$, and $5 \rightarrow 6$ at 626, 642, and 601 nm, respectively. We therefore can write two additional equations:

$$\frac{N_3 A_{31}}{N_4 A_{41}} = \frac{I_F(626)}{I_F(642)} \equiv \alpha \approx 0.113, \quad (23)$$

$$\frac{N_5 A_{56}}{N_4 A_{41}} = \frac{I_F(601)}{I_F(642)} \equiv \beta \approx 0.007. \quad (24)$$

The system of Eqs. (14)–(19), (23), and (24) can be solved to express all populations via the unknown radiationless rates γ_{24} and γ_{61} and the optical pumping rate that is proportional to the laser intensity. The solution for N_3 , N_4 , and N_5 has the form

$$N_k \propto \frac{\gamma_p}{1 + \gamma_p C(\gamma_{24})} \propto \frac{I_{\text{Las}}}{1 + I_{\text{Las}}/I_S^{(6)}(\gamma_{24})}. \quad (25)$$

Since $N_3 A_{31} \propto I_F(626)$, $N_4 A_{41} \propto I_F(642)$, and $N_5 A_{56} \propto I_F(601)$, this solution is equivalent to Eq. (12).

In Fig. 9(b) we compare the calculated saturation intensity for the six-level system $I_S^{(6)}(\gamma_{24}, \gamma_{61})$ with the experimental value I_S^{exp} . First, we set $\gamma_{25} = 0$ and thus neglect the channel that leads to the population of the metastable state 6. The resulting $I_S^{(4)}(\gamma_{24})$ is plotted in Fig. 9 as curve 1. Although the calculated value of $I_S^{(4)}$ decreases with increasing the radiationless rate γ_{24} , it remains significantly larger than the experimentally measured I_S^{exp} . We therefore conclude that the four-level system ignoring the population transfer to the metastable state does not describe our experiment adequately.

Allowing for the finite rates of the radiationless transitions $2 \rightarrow 5$ and $6 \rightarrow 1$ significantly reduces the saturation intensity and makes it compatible with the experimental observations. The rates γ_{23} and γ_{25} can be expressed via γ_{24} and experimental relative line intensities: $\gamma_{23} = \alpha \gamma_{24}$, $\gamma_{25} = \beta \gamma_{24}$. The decay rate of the metastable state γ_{61} remains a free parameter. In Fig. 9 we plot the computed $I_S^{(6)}(\gamma_{24})$ for $\gamma_{61} = 10, 100, \text{ and } 1000 \text{ s}^{-1}$. Only $\gamma_{61} \lesssim 100 \text{ s}^{-1}$ is compatible with the experimentally measured value of I_S .

In principle, the model developed above can be used to calculate the dynamics of the fluorescence yield that is measured in the experiment. However, the number of free parameters remains too large. Besides that, the model is based on the assumption that the dependence of the fluorescence yield on the laser power (saturation intensity) is measured in a steady state, when I_F is not varying in time. In the experiment [18], the secondary sputtering laser pulses were fired at a rate $q = 10 \text{ Hz}$; therefore, the condition $q \ll \gamma_{61}$ was not fulfilled. The time interval between the pulses was too short to reach the steady state.

The model nevertheless demonstrates that the fluorescence yield excited by the cw laser is expected to decrease on a timescale determined mostly by γ_{61} , the rate of the slowest

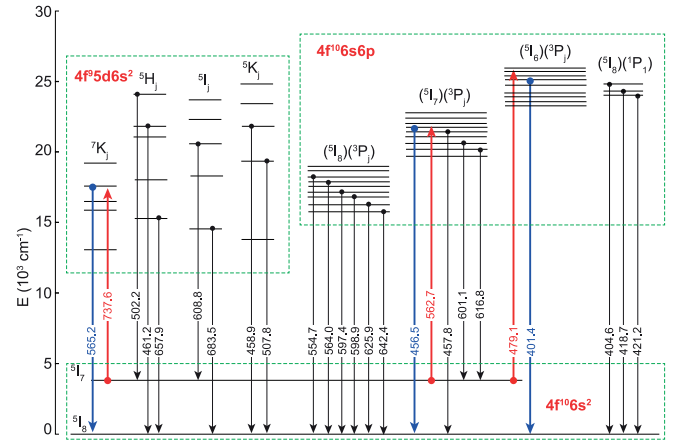


FIG. 10. Energy levels and allowed transitions of Dy [24]. Vertical red and blue arrows indicate the transitions suitable for the repumping from the metastable 5I_7 state to the ground state.

radiationless transition in the system. This rate has the same order of magnitude as the decay rate observed in the experiment after each secondary sputtering laser pulse (Fig. 5). We therefore attribute the observed decay of laser-induced fluorescence to the optical pumping of Dy atoms to the metastable $4f^{10} 6s^2 \ ^5I_7$ state that does not absorb the laser radiation at $\lambda = 458.9 \text{ nm}$.

D. Possible repumping schemes

As discussed in Sec. II E, our data suggest that the pulses of the Nd:YAG laser, in addition to sputtering the nanoparticles, also remove a certain number of atoms from the metastable state and thus enhance the fluorescence yield. Note that the $4f^{10} 6s^2 \ ^5I_7$ state has a large number of strong transitions towards the higher-lying excited states, many of which are strongly broadened and shifted by the interaction with liquid He. Some of these transitions are shown in Fig. 10. For the sputtering laser at $\lambda = 532 \text{ nm}$, the repumping may proceed via the transition at $\lambda_{\text{free}} = 562.7 \text{ nm}$ (see Fig. 10). For the pulsed laser at $\lambda = 355 \text{ nm}$, the repumping probably occurs via another known transition of Dy at $\lambda_{\text{free}} = 357.1 \text{ nm}$ [24].

For a more accurate measurements of the atomic diffusion on a longer timescale and for visualization of the helium flow, it is essential to increase the observation time. This can be achieved by a more efficient repumping scheme using a cw or pulsed laser tuned to the wavelength of one of the transitions originating from the 5I_7 state. Of particular interest are the transitions towards the excited states that can also decay to the ground state via spontaneous emission at another allowed transition. In Fig. 10 we identify three possible repumping schemes: (1) intermediate state 7K_7 , excitation at 737.6 nm ($A_{ki} = 10^5 \text{ s}^{-1}$) and spontaneous emission at 565.2 nm ($A_{ki} = 4 \times 10^5 \text{ s}^{-1}$); (2) intermediate state $(^5I_7)(^3P_2)$, excitation at 562.7 nm ($A_{ki} = 2 \times 10^5 \text{ s}^{-1}$) and spontaneous emission at 456.5 nm ($A_{ki} = 7 \times 10^5 \text{ s}^{-1}$); and (3) intermediate state $(^5I_6)(^3P_2)$, excitation at 479.1 nm ($A_{ki} = 1.2 \times 10^6 \text{ s}^{-1}$) and spontaneous emission at 401.4 nm ($A_{ki} = 2.9 \times 10^6 \text{ s}^{-1}$) or at 404.6 nm ($A_{ki} = 1.9 \times 10^8 \text{ s}^{-1}$).

Scheme 1 uses spectrally narrow inner-shell transitions. However, both transitions involved in this scheme are rather weak, as indicated by their respective $A_{ki} \sim 10^5 \text{ s}^{-1}$. On the other hand, scheme 3 involves much stronger transitions. Although in this case, the excitation spectrum is expected to be strongly broadened. Moreover, this scheme relies on a radiationless quenching of the laser excited state towards closely lying (5I_6)(3P_2) or (5I_8)(1P_1) states that possess especially strong probability of a spontaneous decay towards the ground state.

IV. CONCLUSIONS

Impurity atoms injected into superfluid He and excited by resonant laser radiation can be used as microscopic tracers of the liquid He flow. In particular, atoms of rare-earth elements with their spectrally narrow inner-shell electronic transitions already at a moderate excitation laser power emit a sufficiently bright laser-induced fluorescence that can be used for

imaging. In the case of dysprosium, investigated in the present work, the observation time is strongly limited by the effect of the optical pumping into a metastable 5I_7 state and the associated depletion of the ground state. This finding allows us to explain the previously observed saturation of the Dy absorption line by a relatively weak resonant laser radiation. Our observations set an upper limit to the value of the diffusion coefficient of neutral impurity atoms in superfluid He that is compatible with earlier estimates. We propose to use an additional cw or pulsed laser to optically pump the atoms trapped in the metastable state back into the ground state in order to increase the fluorescence yield and thus achieve a higher sensitivity.

ACKNOWLEDGMENTS

This work was supported by JSPS KAKENHI Grants No. JP24000007 and No. JP17H01145. K.K. has obtained support from MOST, Taiwan (Grant No. 109-2112-M-009-002).

-
- [1] G. P. Bewley, D. P. Lathrop, and K. R. Sreenivasan, *Nature (London)* **441**, 588 (2006).
- [2] M. S. Paoletti, M. E. Fisher, K. R. Sreenivasan, and D. P. Lathrop, *Phys. Rev. Lett.* **101**, 154501 (2008).
- [3] T. V. Chagovets and S. W. Van Sciver, *Phys. Fluids* **27**, 045111 (2015).
- [4] M. LaMantia and L. Skrbek, *Phys. Rev. B* **90**, 014519 (2014).
- [5] P. Švančara, P. Hrubcová, M. Rotter, and M. LaMantia, *Phys. Rev. Fluids* **3**, 114701 (2018).
- [6] W. Kubo and Y. Tsuji, *J. Low Temp. Phys.* **187**, 611 (2017).
- [7] B. Mastracci and W. Guo, *Phys. Rev. Fluids* **3**, 063304 (2018).
- [8] B. Mastracci and W. Guo, *Phys. Rev. Fluids* **4**, 023301 (2019).
- [9] H. Bauer, M. Beau, A. Bernhardt, B. Friedl, and H. J. Reyher, *Phys. Lett. A* **137**, 217 (1989).
- [10] B. Tabbert, M. Beau, M. Foerste, H. Günther, C. Hönninger, H. Hust, K. Layer, G. zu Putlitz, and T. Schumacher, *Z. Phys. B* **98**, 399 (1995).
- [11] W. Guo, J. D. Wright, S. B. Cahn, J. A. Nikkel, and D. N. McKinsey, *Phys. Rev. Lett.* **102**, 235301 (2009).
- [12] W. Guo, S. B. Cahn, J. A. Nikkel, W. F. Vinen, and D. N. McKinsey, *Phys. Rev. Lett.* **105**, 045301 (2010).
- [13] A. Marakov, J. Gao, W. Guo, S. W. Van Sciver, G. G. Ihas, D. N. McKinsey, and W. F. Vinen, *Phys. Rev. B* **91**, 094503 (2015).
- [14] J. Gao, A. Marakov, W. Guo, B. T. Pawlowski, S. W. Van Sciver, G. G. Ihas, D. N. McKinsey, and W. F. Vinen, *Rev. Sci. Instrum.* **86**, 093904 (2015).
- [15] P. Moroshkin, A. Hofer, and A. Weis, *Phys. Rep.* **469**, 1 (2008).
- [16] K. Ishikawa, A. Hatakeyama, K. Gosyono-o, S. Wada, Y. Takahashi, and T. Yabuzaki, *Phys. Rev. B* **56**, 780 (1997).
- [17] Q. Hui and M. Takami, *J. Low Temp. Phys.* **119**, 393 (2000).
- [18] P. Moroshkin, A. Borel, and K. Kono, *Phys. Rev. B* **97**, 094504 (2018).
- [19] P. Moroshkin and K. Kono, *Phys. Rev. B* **99**, 104512 (2019).
- [20] V. Fernandez, A. Garcia, K. Vossoughian, E. Popov, S. Garrett, and J. Eloranta, *J. Phys. Chem. A* **119**, 10882 (2015).
- [21] P. Moroshkin, R. Batulin, P. Leiderer, and K. Kono, *Phys. Chem. Chem. Phys.* **18**, 26444 (2016).
- [22] P. Moroshkin, P. Leiderer, and K. Kono, *Phys. Fluids* **29**, 047106 (2017).
- [23] P. Moroshkin, V. Lebedev, and A. Weis, *Europhys. Lett.* **96**, 26002 (2011).
- [24] A. Kramida, Yu. Ralchenko, J. Reader, and NIST ASD Team, NIST Atomic Spectra Database version 5.3, National Institute of Standards and Technology, Gaithersburg, MD, <http://physics.nist.gov/asd>.
- [25] J. Wilks, *The Properties of Liquid and Solid Helium* (Clarendon, Oxford, 1967).
- [26] G. A. Williams and R. E. Packard, *Phys. Rev. Lett.* **33**, 280 (1974).
- [27] R. J. Donnelly, *Quantized Vortices in Helium II* (Cambridge University Press, Cambridge, 1991).
- [28] D. N. McKinsey, W. H. Lippincott, J. A. Nikkel, and W. G. Rellergert, *Phys. Rev. Lett.* **95**, 111101 (2005).
- [29] K. Fukuda, Y. Hirayoshi, and A. Hirai, *Phys. Lett. A* **47**, 377 (1974).
- [30] N. Piegay, G. Tastevin, and P. J. Nacher, *J. Low Temp. Phys.* **121**, 785 (2000).
- [31] A. Fujisaki, K. Sano, T. Kinoshita, Y. Takahashi, and T. Yabuzaki, *Phys. Rev. Lett.* **71**, 1039 (1993).
- [32] B. Tabbert, M. Beau, H. Günther, W. Häußler, C. Hönninger, K. Meyer, B. Plagemann, and G. zu Putlitz, *Z. Phys. B* **97**, 425 (1995).
- [33] T. Furukawa, Y. Matsuo, A. Hatakeyama, Y. Fukuyama, T. Kobayashi, H. Izumi, and T. Shimoda, *Phys. Rev. Lett.* **96**, 095301 (2006).
- [34] M. Arndt, S. I. Kanorski, A. Weis, and T. W. Hänsch, *Phys. Lett. A* **174**, 298 (1993).
- [35] J. Crank, *The Mathematics of Diffusion* (Clarendon, Oxford, 1975).
- [36] G. H. Duffey, *Modern Physical Chemistry* (Kluwer Academic, New York, 2000).
- [37] I. I. Sobelman, *Atomic Spectra and Radiative Transitions* (Springer, Berlin, Heidelberg, 1979).
- [38] W. Demtröder, *Laser Spectroscopy* (Springer, Berlin, 2008).
- [39] V. A. Komarovskii, *Opt. Spectrosc.* **71**, 322 (1991) [*Opt. Spektrosk.* **71**, 559 (1991)].